MODELING OF SELF-FOCUSING EXPERIMENTS BY BEAM PROPAGATION CODES

W. H. Williams *P. A. Renard*

K. R. Manes *D. Milam*

J. T. Hunt *D. Eimerl*

Introduction

Computer codes that model the propagation of intense laser beams through laser systems have played key roles in the design and analysis of all the ICF lasers built at Livermore.[1] These codes treat, at various levels of sophistication, the effects of linear diffraction, loss, amplification, and beam perturbation by self-focusing.

Laser designs for the National Ignition Facility (NIF)[2] are being analyzed using two recently developed comprehensive, *ab initio* computer simulation codes, PROP1 and PROP2, which treat one and two transverse dimensions, respectively. The codes use fast-Fourier-transform (FFT) propagators on a rectangular grid and treat only one polarization of the field. The effects of linear propagation and nonlinear refraction are calculated separately at each step along the propagation (z) axis. Within the limit of grid resolution, they calculate the electric field experienced by each component in a laser during a shot. To model typical NIF laser operations realistically, we use beam aberrations obtained from measurements on actual optical components, gain profiles from existing testbed amplifiers, adaptive optics models, and characterizations of various optical defects observed in tests of the Beamlet laser.

It is important that these codes be validated, because staging and architecture decisions, which often involve significant cost consequences, are driven by risk-of-damage assessments made using them. Over the past year, PROP1 and PROP2 have been benchmarked against analytical propagation cases, nonlinear perturbation analyses, earlier-generation FFT codes, and, most important, against the results of specially designed experiments. This article describes two comparisons of the code with results of self-focusing experiments conducted in the Optical Sciences Laser (OSL) facility.[3]

Self-focusing has always been a significant problem in fusion lasers, and beam photographs often show intensity ripple generated by self-focusing. Figure 1 demonstrates the seeding of intensity ripple by scattering from obscurations in the chain. These three photographs of the output beam in the Novette laser, the two-beam predecessor of Nova, were taken during shots at 10, 11, and 13 TW. The three intense regions in the right sides of the beams were caused by millimeter-sized imperfections on a turning mirror about two-thirds of the way through the chain. The nonlinear origin of the resulting intensity ripple is apparent from the rapid growth of ripple amplitude with increasing laser power. (The dark band in the center of each beam is the shadow of an absorbing region that separates the

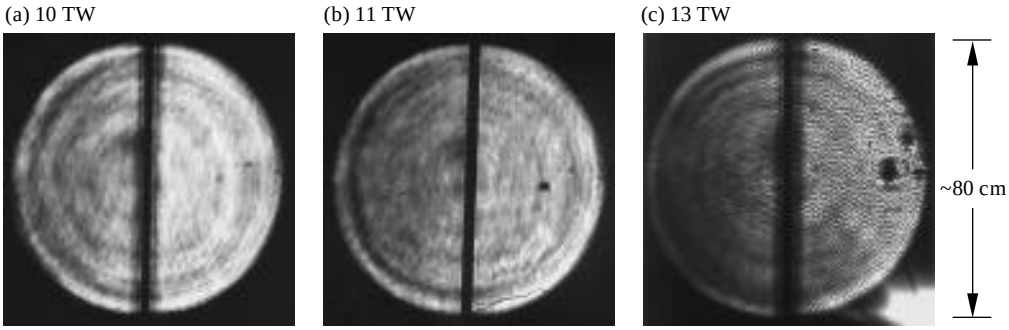

FIGURE 1. Photographs of the output beam of the Novette laser for output powers of 10, 11, and 13 TW. The growth of ripple depth at the three small areas in the right side of the beam illustrates the seeding of self-focusing by imperfections on components in the chain. (70-00-0196-0155pb01)

two halves of the largest amplifier disks to prevent parasitic losses.)

A correct treatment of nonlinear refraction is one of the most difficult aspects of the modeling of beam propagation. The refractive index of most optical materials has a small but important nonlinear (intensity-dependent) contribution that typically limits the high-power performance of fusion lasers. The "nonlinear index coefficient" γ is defined by the expression for the total refractive index,

$$n = n_0 + \gamma I, \tag{1}$$

where n_0 is the linear index and I is the intensity. The optical propagation distance z is related to n_0 and γ and the physical path length d by the rule

$$z = \frac{d}{n_0 + \gamma I} \approx \frac{d}{n_0} - \frac{B}{k}, \tag{2}$$

where $k = 2\pi / \lambda$ is the wave number and B is the intensity-dependent phase retardation, given by

$$B(x, y) = k\gamma \int_0^L I(x, y)\, dz; \tag{3}$$

the integral is taken along a particular ray path through the laser. Intense regions of the beam induce more retardation, causing the wavefront to lag and focus just as a positive lens does.

Localized self-focusing can produce very high intensities. In most simple calculations, the self-focusing at local intensity maxima is treated in Fourier-transform space. The input intensity ripple is described by a Fourier distribution; the self-focusing in a segment of the beam path is described by a multiplication factor, or gain, for each spatial-frequency component in the distribution.[4] Transforming the amplified frequency distribution back to physical space yields the intensity ripple at the output of the path segment. The gain for individual frequency components of the electric field can be as high as $\exp(B)$, and the total induced phase retardation in a laser operated at high intensity can exceed 2π. Therefore, for ripple of the physical scale that corresponds to greatest gain, the power of those components can be increased by a factor of $\exp(2B)^2 \approx 300{,}000$.

A major contribution to our ability to build high-power lasers was the realization that a spatial filter could be used to block the Fourier components of intensity ripple that experienced highest gain.[5] Lenses in the spatial filters also correct for linear diffraction through image relaying.[6,7] The filters are interspersed in the chain so as to "clean" the beam after each accumulation of ΔB in phase retardation; the present NIF design point is $\Delta B = 2.2$ rad. The apertures used in the spatial filters segregate the beam perturbations into high-frequency components, which are blocked, and low-frequency components, which are transmitted.

There remains the problem of understanding the issues that result from modest self-focusing of $\Delta B = 2$–2.3 in sections of the chain between filters. The most serious of these issues is optical damage. Optical damage in the near IR is presumed to depend on the local strength and duration of the optical field and on the condition of the optical component, which in actual systems may depend on its usage history. In most instances, the damage threshold of optical surfaces and coatings is less than that of the bulk material. One task in evaluating a proposed design is to determine the damage thresholds of the various components. A second task is to use a code such as PROP2 to determine the risk of damage for the proposed design. Self-focusing must be considered during this determination. During transmission of a beam at a high (but nominally safe) intensity through an optical component, self-focusing within the component at local regions of high intensity can cause enough intensification to damage the exit surface. In extreme cases, the induced focusing can break the beam into intense filaments that cause internal bulk damage called angel-hair tracking.[8]

Figure 2 illustrates an interesting special case of self-focusing, called hot-image formation. Light diffracted by an obscuration or defect on one component spreads across the beam in a second component. Nonlinear refraction in this second component, driven by the sum of the scattered and primary beams, creates a lensing effect that deflects some of the energy from the beam into a downstream focus, which appears as a bright image of the obscuration. A third component, in the plane of this induced "hot" image, might be damaged even when the system was operating at a nominally safe intensity that did not damage the first two components.

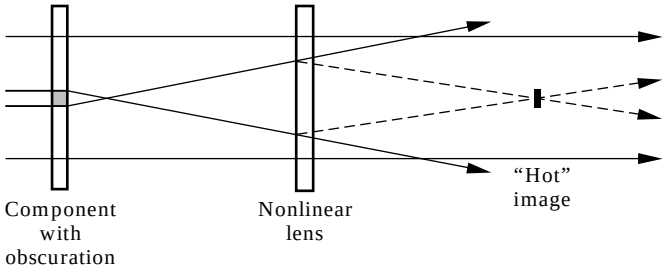

FIGURE 2. Nonlinear refraction induced by the sum of a scattered wave and the intense background wave produces a conjugate wave that is focused to an intense ("hot") image. (70-00-0196-0142pb01)

Hot-image formation by a thin "lens" has been treated analytically for low-intensity ripples in a

high-intensity beam.[9] The scattering sources treated were opaque disks and circular obscurations with Gaussian-distributed opacity. The analysis is readily extended to the case of an opaque linear obscuration (e.g., a wire). Neglecting some details, the model predicts that opaque obscurations cause the formation of hot images with intensity that is greater by a factor of $\sim(1 + B^2)$ than the mean intensity in the beam. For $\Delta B = 2.3$ rad, the predicted relative intensity is ~6.

In contrast to analytic perturbation models, which can easily treat only shallow modulation, PROP1 and PROP2 were designed to treat self-focusing of a beam containing deep intensity ripples. Validation of these codes by modeling the performance of large lasers is difficult, because it is difficult to identify all the source terms for amplitude ripple. We have therefore conducted self-focusing experiments in the OSL facility and compared the results with the predictions of the codes. We used the hot-image configuration for the experiments, since we could induce either a hot image or track damage in the "lens" by varying the obscuration.

Arrangement of the OSL Experiments

The OSL is a 100-J class Nd:glass laser staged to produce 0.5–100-ns pulses that are minimally disturbed by nonlinear refraction in the laser itself. In a typical shot, the fluence is below 0.5 J/cm^2 everywhere in the chain, and the induced phase retardation is less than 0.1 wave ($B = 0.6$). The beam diameter is reduced from 80 to 20 mm at the laser output to increase its intensity.

Figure 3 shows the arrangement used for the self-focusing experiments. The beam was passed through a 25-cm-long silica rod. Obscurations (wires with diameter of 175 or 500 μm) were placed in the beam in a plane 100 cm upstream of the rod. The energy, waveform, and spatial distribution of the beam were measured in the plane of the obscuration. Energy was measured to within 1% by an absorbing-glass calorimeter, and the spatial distribution was recorded by a CCD camera. The waveform was recorded by a Hamamatsu diode and a Tektronix SDC5000 oscilloscope and by a streak camera.

The experiment was arranged to allow recording of the spatial distribution of the beam in planes at a suitable range of distances downstream from the silica rod; the hot images were predicted to lie about 100 cm downstream. Because the area of a CCD camera is about 5×6 mm, the entire 20-mm beam could not be recorded without demagnification, which might have limited the resolution in the records of the small, hot images. Two records were therefore made. One camera, placed directly in the 20-mm-diam beam, recorded a 1:1 image of a 5-mm-diam beam segment isolated by an iris. A second camera recorded an image of the same plane, but with a demagnification of about 2:1. Changing the plane of observation without disturbing the cameras was accomplished by mounting the pick-off optics on a slide rail.

Selection of Wire Diameters

Wire diameters were selected on the basis of calculations done with PROP1. We wanted one wire that produced beam ripple of modest depth, which could be regarded as a perturbation, and another that produced very deep modulation. The experimental results confirm that these calculations give a good overall view of the intensity variation along the entire beam path. Figure 4 shows the predicted evolution of intensity with propagation distance z when a 175-μm-diam wire is placed in a 1053-nm plane-wave beam. The wire was at $z = 0$, and the silica rod was positioned between $z = 105$ and $z = 130$ cm. The input pulse waveform was a 0.5-ns linear ramp with a peak intensity of

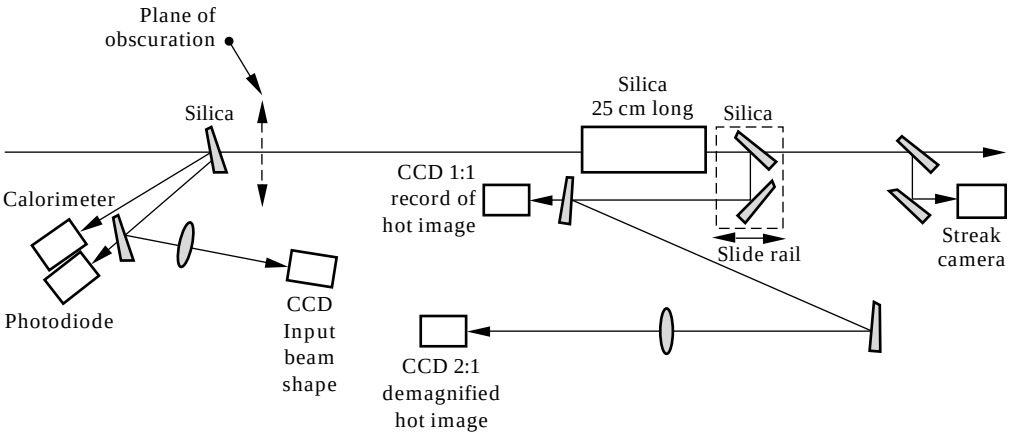

FIGURE 3. Experimental arrangement for characterizing input pulses and recording hot images formed by nonlinear refraction. (70-00-0196-0143pb01)

6.0 GW/cm^2. The waveform was sliced into five equal-fluence segments (with average intensities of 1.3, 3.2, 4.3, 5.0, and 5.6 GW/cm^2), which were independently propagated through the system. The intensity was calculated in planes separated by 5 cm. In each plane, the beam contained the diffraction pattern of the wire; the curve in Fig. 4 simply connects the calculated values of the highest intensity anywhere within the beam.

The calculated intensity increased rapidly in the region immediately beyond the wire as the diffraction ripples formed, and then decreased slightly as the beam propagated to the entrance of the silica rod. Over this zone, intensity changes arose solely from linear diffraction. Self-focusing in the rod produced two effects: the diffraction fringes were narrowed and intensified, and an induced "whole-beam" lensing occurred as a result of the intensity gradients in the superposition of the diffracted light and the main beam. Fringe intensification accounts for the higher intensity at the output end of the rod; high intensity at z = 230 cm was caused by lensing. In this case, the calculated intensity is higher in the hot image than in the rod, and the rod can be regarded as the "lens."

Figure 5 shows the results of a corresponding calculation with a 500-µm-diam wire. The intensity variation within the beam is very high at the entrance of the rod, because the diffracted light has not yet spread across the dark shadow of the wire. It is predicted that fringe intensification will produce a higher intensity at the output surface of the rod than that produced downstream by induced lensing. In this case, it is expected that avoidance of damage to the rod will limit input intensity to values below that required to produce an intense image.

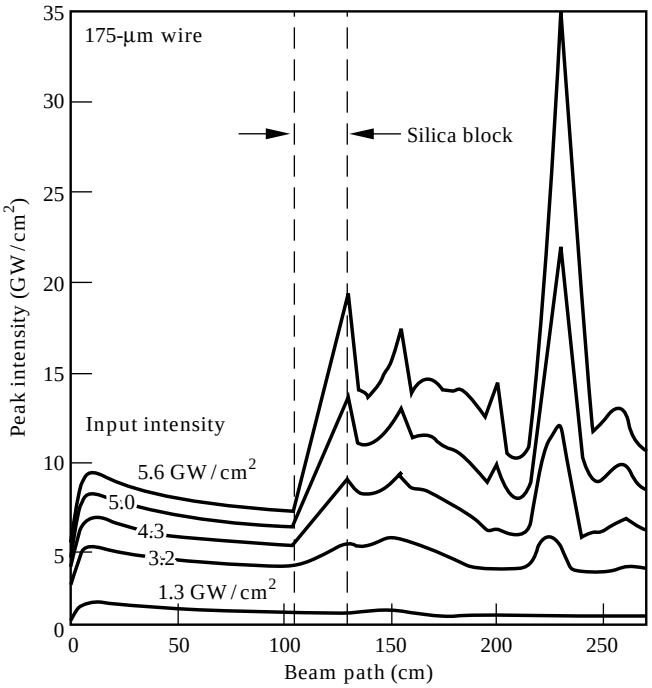

FIGURE 4. Predicted variation of intensity with propagation distance when a plane-wave beam is intercepted by 175-µm-diam wire placed in the beam path and is then propagated through a 25-cm-long silica rod. PROP1 calculations predicted formation of an intense image of the wire. (70-00-0196-0146pb01)

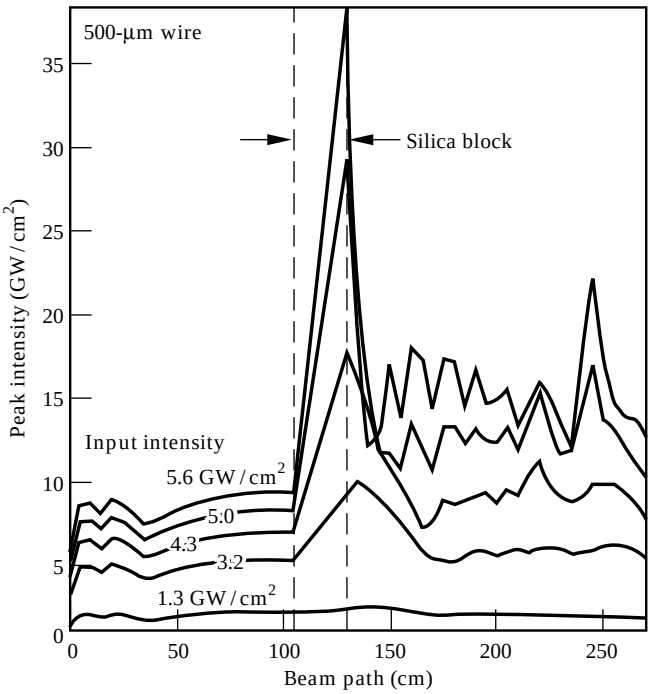

FIGURE 5. Plane-wave PROP1 calculations for a 500-µm-diam wire. The predicted intensity at the output surface of the silica rod is higher than that in the hot image. (70-00-0196-0147pb01)

Results and Analysis

Experiments with each wire diameter were conducted in two stages. In the first series of shots, we held the input intensity approximately constant and recorded the spatial distribution in several planes behind the rod to locate the most intense hot image. In the second series, the plane with the most intense image was recorded as the input intensity was ramped from 1 to 6 GW/cm^2. The duration of the input pulses was about 0.5 ns. The experiments with the 175- and 500-µm-diam wires were modeled with PROP1 and PROP2, respectively.

Experiments with 175-µm Wire

Figures 6–8 show representative data from the experiments with the 175-µm-diam wire. The spatially averaged input fluence was 2.1 J/cm^2. Figure 6 shows the spatial distribution of fluence in the plane containing

the wire. The beam was shaped by apodization and image relaying. It contained weak residual diffraction from the apodization, and random ripple caused by its passage through the many components in the laser. The wire was placed 103 cm in front of the silica rod. Figure 7 shows the 1:1 and 2:1 recordings of the beam in a plane 102 cm behind the rod. The image of the wire is clearly visible. The spatial nonuniformity of the images was caused by intensification due to self-focusing of random intensity fluctuations on the beam. Figure 8 shows the pulse waveform recorded by the streak camera for this shot.

We modeled this experiment with PROP1, using an input beam constructed from the CCD record of the actual input beam. To build an input spatial distribution for the code, we averaged a 4-mm-wide swath across the CCD image of the 20-mm input beam. The wire was modeled as a 175-μm obscuration with four-point smoothing at the edges to minimize Gibbs ringing. The resulting field was propagated across the 103-cm air gap to the rod, through the rod, and through the 102-cm air gap to the plane that was recorded by the output CCD camera. The spatial grid on the field was 8192 points across the 3-cm beam. The rod was divided into ten

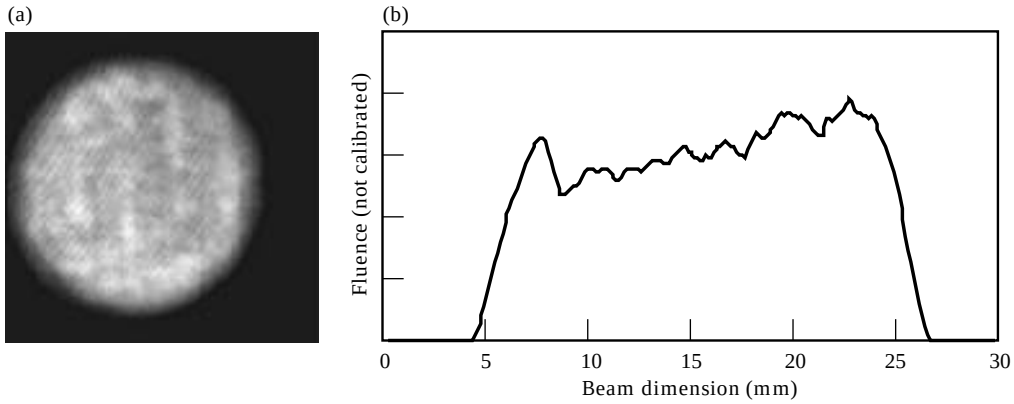

FIGURE 6. (a) CCD record of fluence distribution in the 20-mm-diam beam in the plane of the obscuration. (b) Vertical lineout through the beam. (70-00-0196-0148pb01)

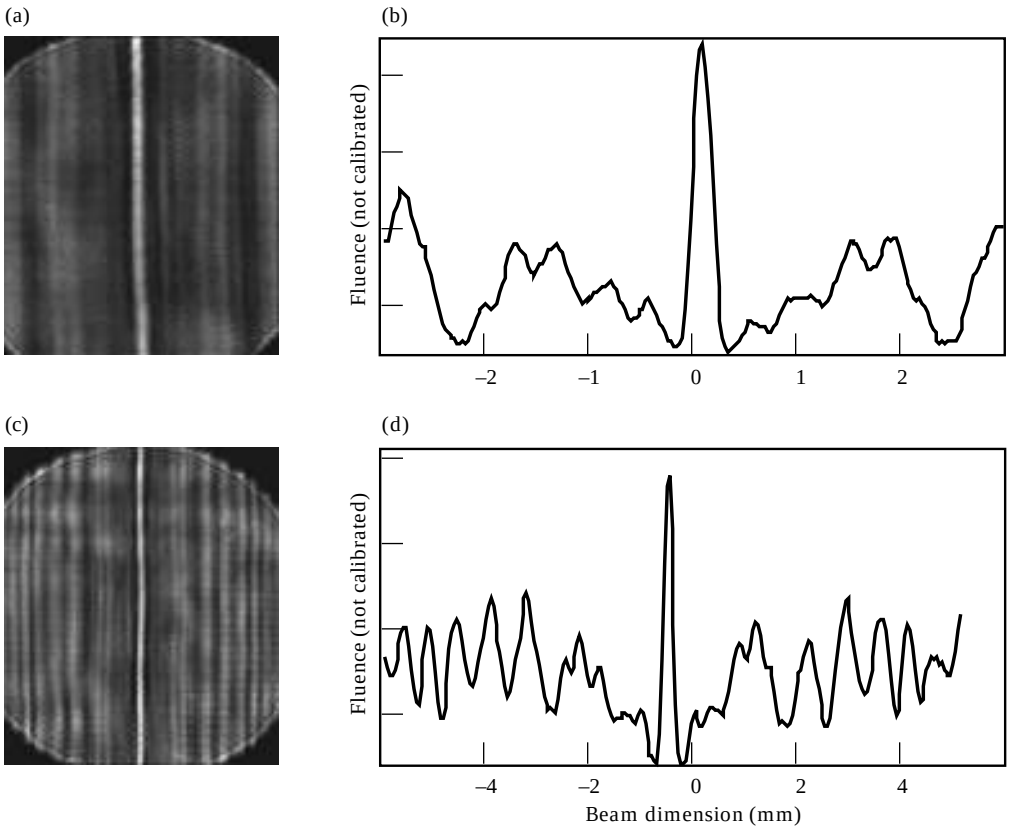

FIGURE 7. Fluence distribution in the hot image of the 175-μm wire, and corresponding horizontal lineouts. Peak input intensity 5 GW/cm^2. (a) and (b), 1:1 record for a central 5-mm-diam area of the beam. (c) and (d), 1.95:1 demagnified image. (70-00-0196-0149pb01)

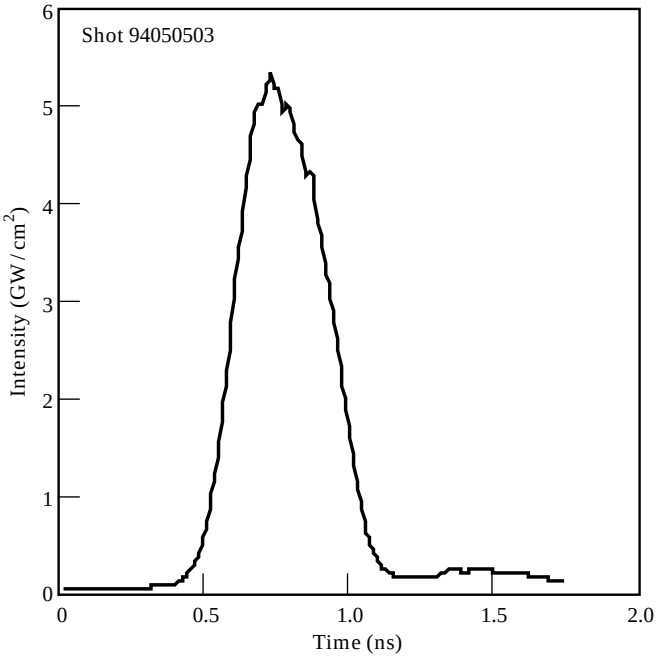

FIGURE 8. Waveform of the input laser pulse. (70-00-0196-0144pb01)

2.5-cm-thick slices, with propagation and self-focusing effects calculated serially in each slice. The value $n_0 = 2.7 \times 10^{-7}$ cm^2/GW was used for the silica.[10] The pulse was divided into 39 time segments of equal duration, which were independently propagated and summed to provide an integrated calculation that could be compared with the relevant 4-mm swath across the time-integrated output CCD image. Figure 9 shows the swaths through the experimental data.

Figure 10 shows the calculated and measured lineouts. To compare the calculation, which yielded a one-dimensional profile with absolute units of J/cm^2, with the relative fluence in the CCD hot-image record, we rescaled the calculated result using a simplex multivariable routine to minimize the rms point-to-point difference between the measured and calculated lineouts. The central peak of the hot image was not included in this minimization. It was necessary to make a small horizontal expansion of the modeled data to bring it into agreement with the measured result. We believe that the horizontal mismatch arose from a small error in the measured 2:1 demagnification of the experimental data.

The intensities in the hot image agree with theory to within 15%. This uncertainty is acceptable, because the resolution of the image of the wire is limited (three pixels at the peak), because the uncertainty in the nonlinear refractive index of the silica is about 10%, the uncertainty in the measurement of spatially averaged

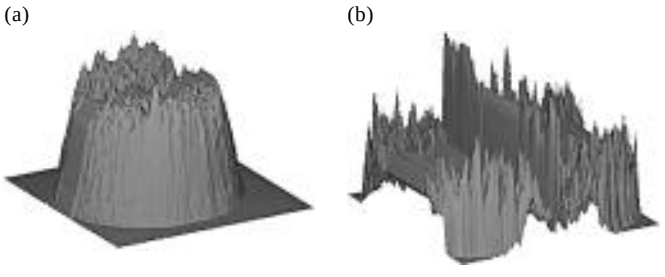

FIGURE 9. Averaged 4-mm-wide swaths across the CCD records of (a) the input beam and (b) the hot image used in PROP1 modeling of the experiments with the 175-μm wire. (70-00-0196-0145pb01)

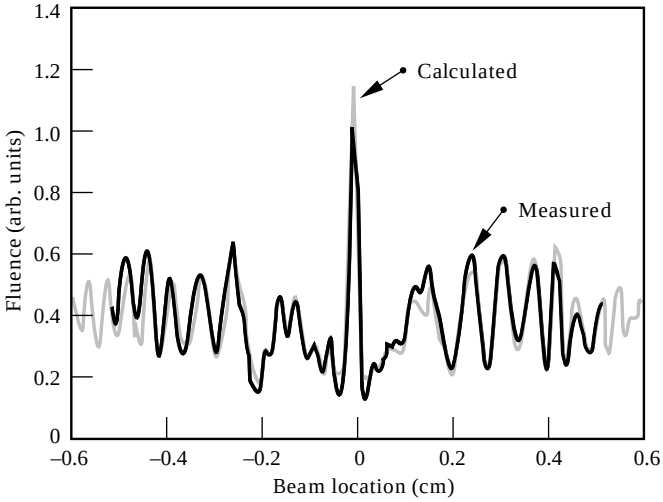

FIGURE 10. Calculated and measured fluence distributions in the hot image of the 175-μm wire. (70-00-0196-0150pb01)

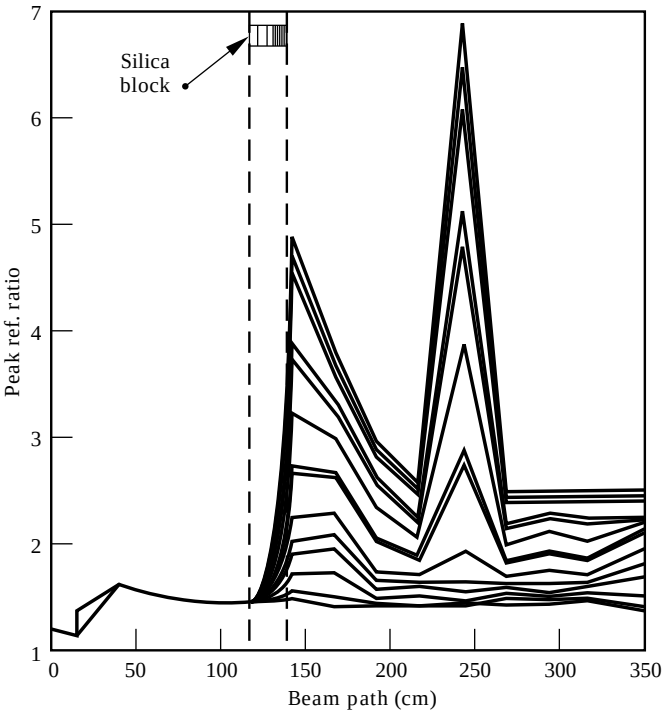

FIGURE 11. Calculated intensity vs propagation distance for time slices for the experiment with the 175-μm wire. (70-00-0196-0151pb01)

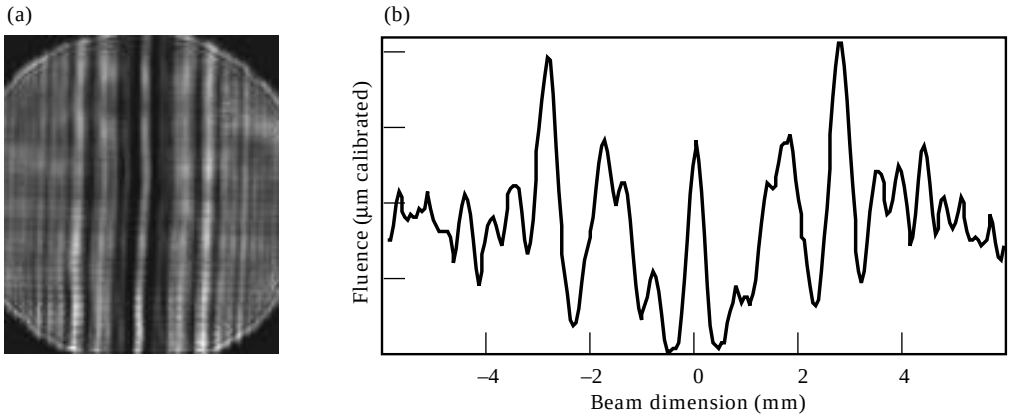

FIGURE 12. Fluence distribution in the image plane for a 500-μm wire. Intensity in the image was less than that in adjacent diffraction fringes. (70-00-0196-0152pb01)

intensity is at least 5%, and the hot-image intensity scales approximately as B^2. Further, the output CCD record contains random intensity variations as well as the image of the wire. We conclude that experiment and theory are in excellent agreement.

It should be noted that time-integrated records such as those in Fig. 10 do not show the hot-image intensity generated at the temporal peak of the pulse. Figure 11 shows the calculated intensity vs z for about half of the time slices. During the most intense slice, the intensity in the hot image was 7 times the mean intensity in the main beam. The intensity for this slice was about 5 GW/cm^2, and the phase retardation was B = 2.0 rad. Thus the intensification for this slice was greater than the factor of $1 + B^2 = 5$ predicted by the analytic perturbation models for shallow ripple.

Experiments with 500-μm Wire

The experiment was repeated with a 500-μm wire 105 cm in front of the rod. Figure 12 shows one of the images of a plane 103 cm behind the rod, recorded during a shot with a fluence of 2.3 J/cm^2. The image of the wire is visible, but its intensity is less than that of the adjacent diffraction ripples. This was the case for shots at lower fluence and for images in other planes. Track damage was induced in the rod by this shot. The spatially averaged intensity at the temporal peak of the pulse was 5 GW/cm^2, and the intensity was higher by 10–15% at isolated places in the beam.

PROP 2 was used to model the tracking induced in this experiment. The CCD image of the input beam was placed on a 3×3 cm grid of 2048×512 pixels, with the higher resolution in the direction orthogonal to the obscuring wire. The rod was broken into three 5-cm slices and ten 1-cm slices, with ten propagation steps in each slice. The thicker 5-cm slices were acceptable at the entrance of the rod, because the intensity increased slowly there. Because track induction is a response to instantaneous intensity, we did not integrate over the intensity range in the temporal waveform. Instead, several runs were made with the input beam scaled to yield spatially averaged intensities between 1.9 and 7.5 GW/cm^2.

Figure 13 shows the results of the calculations as plots of the highest intensity in the rod, anywhere in the beam, vs distance through the rod. For high input intensity, there is a value of z for which the intensity increases abruptly. The apparent stabilization of intensity at high values after the abrupt rise is an artifact of the calculation that occurs when the area of individual intense filaments in the beam is less than the area of the grid sectors.

Damage should occur in the rod where intensities are above the bulk damage threshold. The nonzero rise time of the temporal waveform and the value of the damage threshold both play roles in shaping the damage. As the intensity increases during the rise of the pulse, the z value for the abrupt increase in intensity decreases, so the zone of high intensity starts at the rear surface of the rod and moves toward the front. If the intensity in the self-focused filaments in the beam

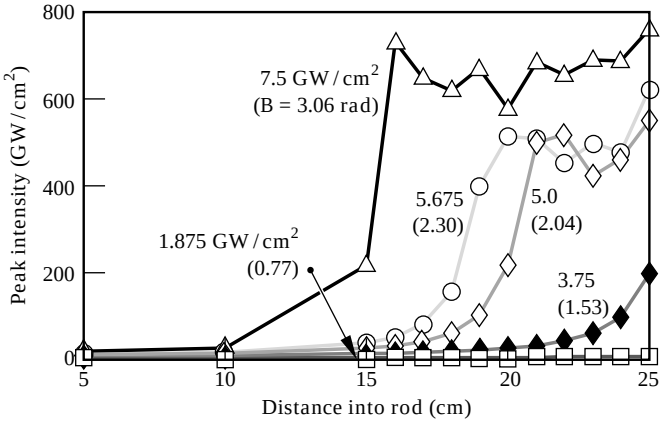

FIGURE 13. Calculated intensity vs propagation distance within the silica rod for the experiment with the 500-μm wire. The intensity distribution in the input beam was scaled to have spatially averaged values of 1.9 to 7.5 GW/cm^2; that for the experiment was 5 GW/cm^2. (70-00-0196-0153pb01)

exceeds the damage threshold, the result is the familiar angel-hair track damage. The value of the bulk damage threshold would play a significant role in determining the length of the track if one were attempting to determine the minimum input intensity for track induction, because of the slow variation of intensity with z at relatively low input intensities (see the calculation for 3.75 GW/cm^2 in Fig. 13). At input intensities well above the minimum for tracking, however, the intensity rises so abruptly that the value of the damage threshold is almost irrelevant. For 0.5-ns pulses, the damage threshold is between 300 and 500 GW/cm^2 (Ref. 11), so the calculated intensities are adequate to cause damage.

There is remarkable agreement between the length of the tracks induced in the rod and corresponding features of the PROP2 calculations. The tracks begin 18 cm from the entrance face; the calculations predict that the abrupt increase in intensity occurs 18–20 cm from the entrance of the rod for intensities of 5.0 to 5.6 GW/cm^2, which is a reasonable representation of the variation of input powers in the experiment. There is also good agreement between the predicted shape of the beam at the output of the rod (Fig. 14) and the pattern of damage on that face. The most intense spikes in Fig. 14 are in two rows separated by 2.3 mm and concentrated in the top of the beam. The damage in the rod shows the same top-to-bottom spatial asymmetry in the magnitude of the damage, and it contains two principal rows of spikes separated by 2.5 mm.

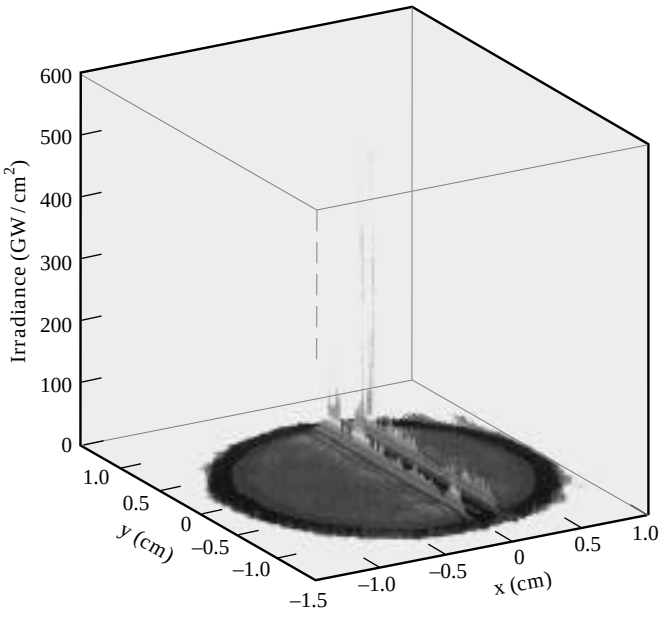

FIGURE 14. Calculated flux distribution at the output face of the rod for B = 2 rad and for spatially averaged intensity 5 GW/cm^2 at the plane of the 500-μm wire. The top-to-bottom asymmetry in spike intensity correlates with the fluence variation in the input beam (see Fig. 6). (70-00-0196-0154pb01)

Summary

We have used the PROP1 and PROP2 codes to model self-focusing experiments conducted in the OSL facility. The source terms, both native beam ripple and that induced by obscurations, were measured and used in the codes. We accurately calculated the shape of an induced "hot" image formed by placing a thin wire in the beam, and the length of self-focusing tracks induced by placing a thicker wire in the beam. These results provide a significant validation of the codes.

Acknowledgments

We are indebted to John Trenholme and Clay Widmeyer for valuable input during the design of the experiment and the reduction of the data, and to Walter Sell, who maintained and operated the OSL facility during the experiments.

Notes and References

1. The earlier codes BTGAIN, ZAX, SNORT, LAMP, ARTEMIS, and MALAPROP, which were developed at Livermore, are reviewed in W. W. Simmons, J. T. Hunt, and W. E. Warren, "Light Propagation Through Large Systems, " *IEEE J. Quantum Electron.* QE-17, 1727–1743 (1981). Liberal use was also made of the code OASIS, originally developed by Rockwell Rocketdyne, Inc. under contract with the U.S. Air Force.
2. J. A. Paisner, E. M. Campbell, and W. J. Hogan, "The National Ignition Facility Project," Lawrence Livermore National Laboratory, Livermore, CA, UCRL-JC-117379 Rev. 1 (June 1994).
3. D. Eimerl, R. Boyd, and D. Milam, "The OSL: A New Facility for Laser Research," *ICF Quarterly Report* 1(3), 108–113, Lawrence Livermore National Laboratory, Livermore, CA UCRL-LR-105821-91-3 (1991).
4. V. I. Bespalov and V. I. Talanov, "Filamentary Structure of Light Beams in Nonlinear Liquids," *JETP Lett.* 3, 307–312 (1966).
5. W. W. Simmons, S. Guch, F. Rainer, and J. E. Murray, "High-Energy Spatial Filter for Removal of Small-Scale Beam Instabilities in High-Power Lasers," *IEEE J. Quantum Electron.* QE-11, 300 (1975).
6. J. T. Hunt, P. A. Renard, and W. W. Simmons, *Appl. Opt.* 16, 779–782 (1977).
7. J. T. Hunt, J. A. Glase, W. W. Simmons, and P. A. Renard, *Appl. Opt.* 17, 2053–2057 (1978).
8. J. A. Fleck, Jr., and C. Layne, *Appl. Phys Lett.* 22, 467–469 (1973).
9. J. T. Hunt, K. R. Manes, and P. A. Renard, *Appl. Opt.* 32, 5973–5982 (1993).
10. D. Milam and M. J. Weber, *J. Appl. Phys.* 47, 2497–2501 (1976).
11. E. W. Van Stryland, M. J. Soileau, A. L. Smirl, and W. E. Williams, *Phys. Rev. B* 23, 2144–2151 (1980).